

# Self-Aligned Hybrid Nanocavities Using Atomically Thin Materials

Chee Fai Fong,\* Daiki Yamashita, Nan Fang, Shun Fujii, Yih-Ren Chang, Takashi Taniguchi, Kenji Watanabe, and Yuichiro K. Kato\*



Cite This: *ACS Photonics* 2024, 11, 2247–2254



Read Online

ACCESS |



Metrics & More



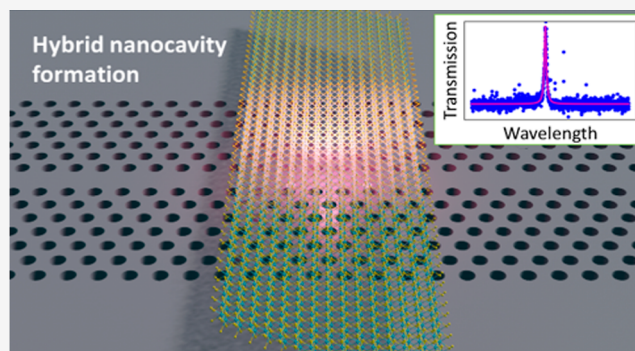
Article Recommendations



Supporting Information

**ABSTRACT:** Two-dimensional (2D) materials are increasingly being adopted in hybrid photonics via integration with photonic structures, including cavities. The utility of 2D materials for dielectric environment engineering in hybrid nanophotonic devices remains largely unexplored. We demonstrate self-aligned hybrid nanocavities in which 2D material flakes are used to form cavities locally wherever they are placed along the PhC waveguide postfabrication. We successfully fabricated such hybrid nanocavities with various 2D materials on silicon PhC waveguides, obtaining  $Q$  factors as high as  $4.0 \times 10^5$ . Remarkably, even monolayer flakes can provide sufficient local refractive index modulation to induce high  $Q$  nanocavity formation. We have also observed cavity PL enhancement in a self-aligned  $\text{MoTe}_2$  cavity device with an enhancement factor of about 15. Our results highlight the prospect of using such 2D material-induced PhC nanocavities to realize a wide range of photonic components for hybrid integrated photonic circuits.

**KEYWORDS:** photonic crystal, hexagonal boron nitride, transition metal dichalcogenide, light–matter interaction



## INTRODUCTION

Two-dimensional (2D) van der Waals layered materials such as graphene, hexagonal boron nitride (hBN), and transition metal dichalcogenides (TMDCs) are garnering significant attention for both fundamental science and device applications.<sup>1–7</sup> In particular, semiconducting TMDCs have a direct band gap at monolayer thickness.<sup>8,9</sup> They exhibit bright optical emission which is governed by their exciton (Coulomb-bound electron–hole pair) responses even up to room temperature due to the large exciton binding energies of hundreds of meV.<sup>10</sup> Many 2D materials exhibit large optical nonlinearities,<sup>11</sup> which could also be intricately linked to the valley polarization.<sup>12,13</sup> The amenability to strain and defect engineering also makes 2D materials promising for the creation of emitters for quantum light sources.<sup>4,6,14</sup>

The integration of 2D materials with nanophotonic architectures<sup>15–27</sup> offers a promising avenue to manipulate light–matter coupling, thereby facilitating the realization of hybrid devices such as lasers,<sup>28–30</sup> quantum emitters,<sup>31,32</sup> and photodetectors.<sup>22,33,34</sup> To achieve optimal device performance, it is imperative to couple 2D materials with cavities exhibiting a high quality factor over the mode volume ratio ( $Q/V_{\text{mode}}$ ). The planar air hole photonic crystal (PhC) nanocavities<sup>35–37</sup> promise strong light confining in an ultrasmall mode volume, rendering them highly attractive for the aforementioned hybrid device applications.

In previous studies, the conventional approach to hybrid devices involved the transfer of 2D materials, such as TMDC

mono- and few-layer flakes onto prefabricated nanocavities. Despite being ultrathin, the transfer of a TMDC flake alters the dielectric environment of the cavity and could induce other optical losses which results in significant degradation in the cavity quality ( $Q$ ) factor.<sup>34,38,39</sup> Interestingly, the impact of the TMDC flake on the dielectric environment is usually ignored or regarded as a small perturbation that needs to be slightly compensated for by adjusting the design of the nanophotonic cavity. The potential of 2D materials for dielectric environment engineering in hybrid nanophotonic devices is still largely untapped. Instead of being a detriment, the change in the dielectric environment caused by the 2D material can be utilized to enable alternative methods for enhanced cavity light–matter coupling.

In this work, we demonstrate self-aligned hybrid nanocavities in which 2D material flakes are used to form cavities locally wherever they are placed along the PhC waveguide postfabrication. The presence of the flake modulates the local refractive index, changing the waveguide dispersion, leading to optical confinement and thus cavity formation. We successfully

**Received:** December 30, 2023

**Revised:** May 8, 2024

**Accepted:** May 8, 2024

**Published:** May 17, 2024



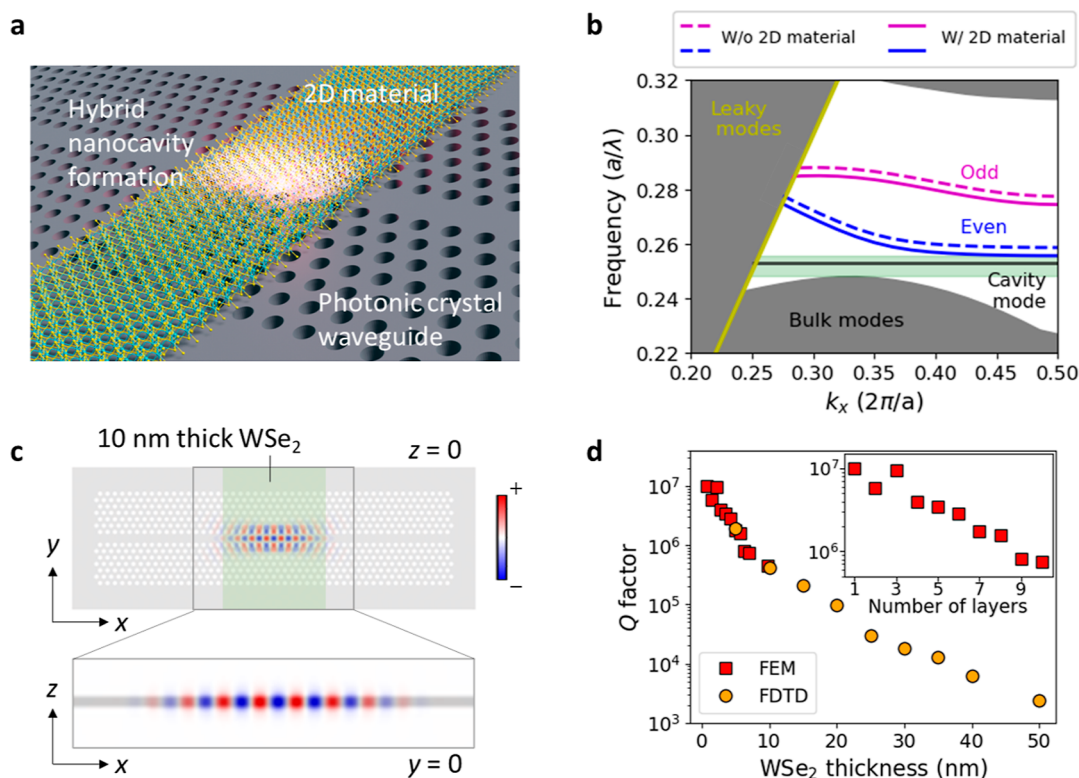


**Figure 1.** 2D material hybrid PhC mode gap nanocavity. (a) Schematic of a device structure showing cavity formation at the location of the 2D material. (b) Photonic bands of the PhC waveguide showing the odd and even guided modes as labeled, as well as the mode gap in green and the cavity mode within. The solid (dashed) lines represent the guided modes with (without) the 2D material. (c) Electric field  $E_y$  profile of the cavity mode in the  $xy$ - and  $xz$ -planes. The green shaded region represents the 2D material flake. (d) Dependence of the cavity  $Q$  factor against thickness of  $WSe_2$ . (Inset) Plot of the  $Q$  factor against the number of layers.

fabricated such nanocavities with various 2D materials including hexagonal boron nitride (hBN), tungsten diselenide ( $WSe_2$ ), and molybdenum ditelluride ( $MoTe_2$ ), achieving high  $Q$  factors of  $10^4$  to  $10^5$ . Remarkably, we discovered that even a monolayer flake could give rise to sufficient local refractive index modulation to form a hybrid nanocavity. In fact, according to simulation results, the thinner the flake, the more moderate the spatial modulation of the refractive index, the higher the  $Q$  factor. In such hybrid systems, the monolayer represents the extreme limit of index modulation, promising cavities with high  $Q$  factors. As the flake is spatially self-aligned to the cavity, we have further observed the self-aligned coupling of  $MoTe_2$  photoluminescence (PL) in a hybrid nanocavity device, giving rise to enhanced emission and a lifetime reduction of about 15 times. Our results demonstrate the utility of 2D materials for dielectric environment engineering to create functional hybrid devices, with potential applications in hybrid photonic integrated circuits.

**Design of Hybrid Nanocavity.** For simulating our device structure, we employ the air-suspended W1 line defect PhC waveguide<sup>40</sup> made of silicon (refractive index,  $n_{Si} = 3.48$ ), consisting of a triangular array of air holes with lattice period  $a$ , with a 2D material flake covering a section of the waveguide (Figure 1a). We typically consider a PhC waveguide with 48 and 14 air holes along the  $\Gamma$ - $K$  and  $\Gamma$ - $M$  directions, respectively, with the air hole radius,  $r = 0.28a$  and  $a = 340$  nm. The PhC slab thickness is 200 nm. The photonic band structure of the transverse-electric-like (TE-like) modes of the PhC waveguide is shown in Figure 1b. There are two guided

modes, termed odd and even in accordance with the symmetry of the  $E_y$  field distribution about the  $x$ -axis.

When a 2D material flake is present on the PhC waveguide, the local effective refractive index increases, red-shifting the frequencies of the guided modes. The frequency mismatch between the regions with and without the 2D material flake gives rise to field confinement and thus cavity formation. There are corresponding cavity modes for each of the guided modes in the near-infrared (NIR) regime. The frequencies of the resulting hybrid nanocavity modes are usually lower than the band edge (frequency at  $k_x = 0.5$ ) of the corresponding guided modes. The even cavity modes exhibit much higher  $Q$  factors as the modes are within the mode gap—the frequency range between the even guided mode edge and the lower edge of the photonic band gap (green region in Figure 1b). In this work, we will mainly focus on even cavity modes.

To investigate the cavity mode properties, we consider a rectangular  $WSe_2$  flake (refractive index,  $n_{WSe_2} = 3.95$ <sup>41</sup>) of 10 nm thickness with a lateral width of  $14a$ , partially covering the surface of the PhC waveguide. The flake is assumed to cover the PhC structure completely along the  $y$ -direction. The simulated  $E_y$  field amplitude profile of the fundamental (i.e., lowest energy) even cavity mode is shown in Figure 1c. The cavity mode profile is largely reminiscent of the even guided mode profile, and it remains similar for the range of  $WSe_2$  thicknesses considered in our simulations.

The simulated fundamental cavity mode  $Q$  factor dependence on the thickness of the  $WSe_2$  flake is summarized in Figure 1d. At a thickness of 30 nm, the cavity  $Q$  is about  $1 \times 10^4$ . As the thickness of the  $WSe_2$  flake decreases, the  $Q$  factor

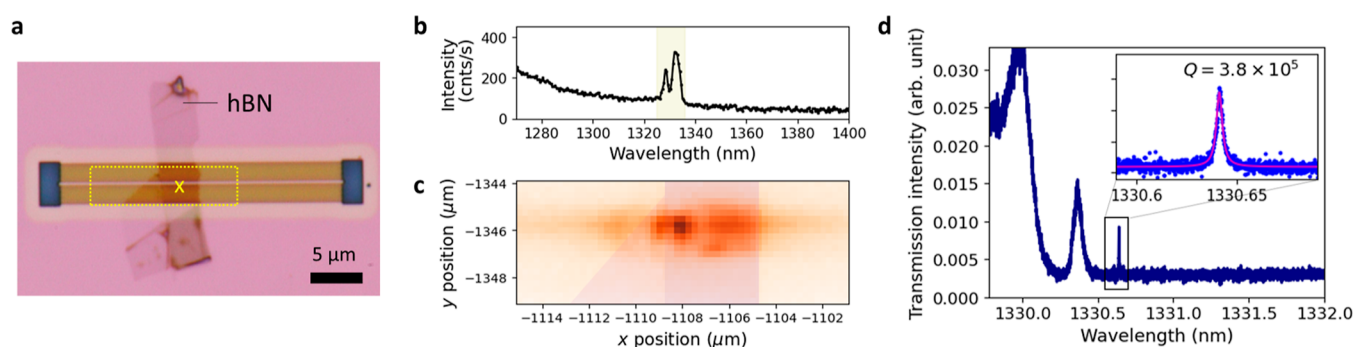


**Figure 2.** hBN-induced hybrid nanocavity. (a) Optical micrograph of an hBN hybrid nanocavity device. The scale bar represents 5  $\mu\text{m}$ . The “x” symbol marks the location of the PL measurement in (b). The dotted box outlines the area of the 2D imaging shown in (c). (b) PL spectrum showing signatures of cavity emission. (c) 2D image of the integrated PL intensity over the wavelength range of 1325–1336 nm showing localized cavity emission at the hBN flake (the flake is indicated by the darkened region). (d) Transmission spectra showing the cavity peak. (Inset) A closer look at the narrow peak fitted to a Lorentzian function (magenta line).

increases, reaching a theoretical value as high as  $10^6$  for few-layer flakes. Simulation results indicate that not only can a monolayer form a cavity but also it promises an ultrahigh  $Q$  factor of the order of  $10^7$ . The atomically thin nature of the flake induces a more gradual transition in the refractive index both vertically along the PhC slab/2D material/air interface and the edges of the 2D materials. Sudden changes in the refractive index can give rise to optical fields with wavevector components falling within the leaky region in momentum space.<sup>42</sup> Consequently, a thin flake introduces a “gentle” perturbation to the fields, reducing the number of components within the leaky region (refer to Supporting Information Figure S1). Compared to thicker flakes, a thinner flake also gives larger refractive index contrast in the PhC slab/2D material/air interface, thus resulting in better confinement of optical fields. These effects lead to diminished loss through coupling to free space, resulting in ultrahigh  $Q$  factors. The dependence of the cavity wavelength, mode volume, as well as the ratio of the field intensity at the PhC surface to the maximum mode field intensity on the WSe<sub>2</sub> flake thickness is provided in Supporting Information Figure S1. For a given set of PhC waveguide parameters and flake width, there is an optimum refractive index modulation to obtain a hybrid nanocavity with the optimum  $Q$  factor, which occurs at different thicknesses for different 2D materials (see Supporting Information Figure S2). Further details about other factors that affect the cavity  $Q$  factor such as the flake lateral width and refractive index are also provided in Supporting Information Figure S2.

**hBN-Induced Hybrid PhC Nanocavity.** Dielectric hBN—which is often used to encapsulate TMDC to prevent exposure to air—is also a suitable 2D material to form hybrid nanocavities. In particular, high crystal quality hBN flakes with low defect densities promise high  $Q$  factors. Figure 2a shows an optical micrograph of a fabricated hBN-on-PhC waveguide device. The PhC slab thickness is 200 nm, and the waveguide consists of 96 and 14 air holes along the  $\Gamma$ – $K$  and  $\Gamma$ – $M$  directions, respectively. The lattice and the air hole radius are  $a = 360$  nm and  $r = 0.27a$ , respectively. The hBN flake is transferred onto the PhC waveguide postfabrication. The thickness of the hBN flake is estimated to be about 20 nm based on the optical contrast, and its lateral width measured along the waveguide is about 12  $\mu\text{m}$ .

By optically exciting the silicon PhC device above the band gap, the weak emission from the silicon substrate can couple to

the guided and/or cavity modes, manifesting as peaks in the PL spectra. For this particular sample, emission peaks appear near the frequency of the even guided mode edge (Figure 2b). By performing 2D PL imaging, we confirm that the emission peaks only appear when excited at the hBN flake along the waveguide, further indicating the formation of a cavity (Figure 2c). The nonuniformity of the 2D PL intensity map could be due to the nonuniformity of the flake and also the presence of multiple cavity modes with different mode profiles (see Supporting Information Figure S5). The polarization properties of the peak are broadly consistent with expectations in accordance with the mode profile (see Supporting Information Figure S3). However, the actual line width of the peaks, and thus the  $Q$  factors, cannot be determined using the spectrometer due to insufficient resolution.

We then carried out transmission measurements by exciting at the hBN flake and detecting the scattered light from the semicircular outcoupler to the right of the waveguide. A few features can be seen in the transmission spectrum (Figure 2d): the guided mode edge can be seen at about 1330.00 nm, as well as a relatively broad peak centered at 1330.34 nm and a narrow peak at 1330.61 nm. The broad peak has a line width of 60.2 pm, corresponding to  $Q = 2.2 \times 10^4$  while the narrow peak has a line width of 3.54 pm, giving  $Q = 3.8 \times 10^5$ . Given the relative position and the  $Q$  factors of the peaks, the narrow and broad peaks should correspond to the fundamental and first higher-order cavity modes.

The extracted  $Q$  factors from the resonant peaks of the transmission spectra are the so-called loaded  $Q$  factors which consist of the intrinsic cavity  $Q$  ( $Q_i$ ) and cavity–waveguide coupling  $Q$  ( $Q_c$ ):<sup>42</sup>  $\frac{1}{Q_l} = \frac{1}{Q_i} + \frac{1}{Q_c}$ . For this hBN device, by changing the transmission measurement configuration to excite at the left output coupler and detecting light from the right output coupler, we are able to observe the resonant dip that corresponds to the absorption of light by the cavity, allowing us to calculate  $Q_i$  of this device to be about  $4.2 \times 10^5$  (Supporting Information Figure S4). Overall, our results show that the flake and the nanocavity are colocalized, essentially forming a self-aligned device. The enhanced Si PL emission also indicates a cavity light–matter coupling.

**Hybrid PhC Nanocavities Using Atomically Thin WSe<sub>2</sub>.** Compared with hBN, it is easier to obtain and identify mono- and few-layer flakes with TMDCs. Motivated by our simulation results, we conduct experiments using WSe<sub>2</sub> as it is

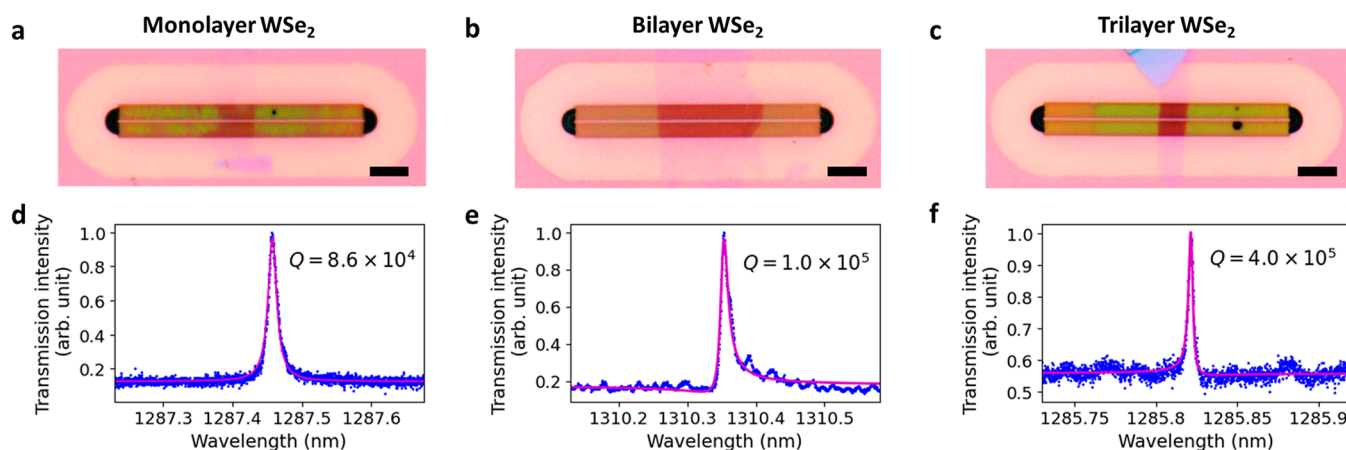


**Figure 3.** Mono- and few-layer WSe<sub>2</sub> hybrid nanocavity. (a–c) Optical micrograph of mono-, bi-, and trilayer WSe<sub>2</sub>-induced nanocavity device. The waveguide consists of 96 and 14 air holes along the  $\Gamma$ – $K$  and  $\Gamma$ – $M$  directions, respectively, to facilitate ease of 2D material flake transfer. The brightness and contrast of the images have been adjusted to improve the visibility of the WSe<sub>2</sub> flake. For the mono- and trilayer device, the PhC waveguide has  $a = 348$  nm while the bilayer device is of  $a = 356$  nm. The lateral widths along the waveguide of the monolayer, bilayer, and trilayer flakes of the devices are  $13a$ ,  $36.5a$ , and  $10a$ , respectively. The cavity resonance of the bilayer device appears at a longer wavelength since the PhC lattice period is larger. The slightly longer cavity resonant wavelength of the monolayer device can be attributed to the larger flake width. Some residues could be left on the sample during the transfer process in the monolayer device. However, there is no significant effect on the transmission spectra. (d–f) Corresponding cavity peak in the transmission spectra for each of the devices. The transmission measurements are performed by exciting the left output coupler and detecting at the right output coupler for the mono- and trilayer devices. As for the bilayer device, the laser excitation is focused on the sample and the transmitted signal is detected at the right output coupler. The peak in (d) is fitted with the Lorentzian function, while the peaks in (e,f) are fitted with the Fano resonance. The scale bars in (a–c) represent  $5 \mu\text{m}$ .

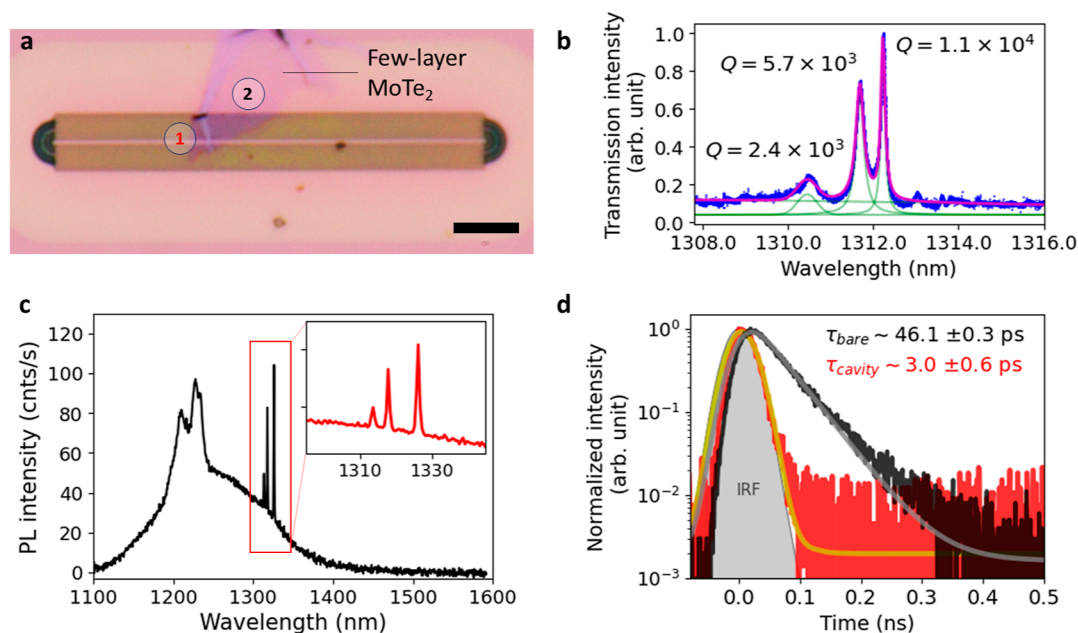


**Figure 4.** PL enhancement in the MoTe<sub>2</sub> hybrid nanocavity. (a) Optical micrograph of the MoTe<sub>2</sub> nanocavity device. The scale bar indicates  $5 \mu\text{m}$ . (b) Transmission spectra obtained by exciting at the left and detecting at the right output coupler, showing the cavity peaks. The green curves are the individual Lorentzian fits, and the magenta curve is the cumulative fit. (c) PL spectrum showing the emission from the MoTe<sub>2</sub> and cavity. (Inset) A zoom-in of the region with the cavity emission peak. (d) Time-resolved PL decay curves of the emission from the cavity and the bare MoTe<sub>2</sub> flake [positions 1 and 2 in (a), respectively] showing the reduced lifetime due to the cavity effect. The cavity and the bare MoTe<sub>2</sub> emission decay curves are fitted using a single and double exponential reconvolution function, respectively. The gray shaded region shows the IRF.

relatively stable in air. The discussion here will focus on a selection of three exemplary devices with monolayer, bilayer, and trilayer flakes (Figure 3). The transmission spectrum for each device is shown in Figure 3e,f. The cavity peaks appear at the expected wavelengths in accordance with the PhC waveguide lattice period. Due to intermode scattering, there is nonzero transmission signal even at frequencies below (i.e.,

wavelengths above) the transmission edge. The interference of this background transmission signal with the cavity peak could result in an asymmetric line shape. By fitting the peaks to either the Lorentzian (symmetric line shape) or Fano resonance (asymmetric line shape),<sup>43</sup>  $Q_1$  is determined to be  $8.6 \times 10^4$ ,  $1.0 \times 10^5$ , and  $4.0 \times 10^5$  for the monolayer, bilayer, and trilayer devices, respectively. Only for the bilayer sample are we able to

obtain the necessary transmission spectra with the cavity resonant dip and peak in the different measurement configurations to extract the  $Q_i$  to be about  $3.7 \times 10^5$ . The cavity  $Q$  factors do not show an obvious increase with the decrease in flake thickness even after considering the flake lateral widths. Various loss mechanisms could affect the extracted  $Q$  factors; further descriptions of the possible mechanisms are provided in the Discussion section. Our results here show unambiguously that even a monolayer flake could give rise to sufficient local refractive index modulation to form a high  $Q$  hybrid nanocavity, despite being only one-atom thick.

**Cavity PL Enhancement in Self-Aligned Hybrid Nanocavity with MoTe<sub>2</sub>.** MoTe<sub>2</sub> is optically active in the NIR, making it an ideal TMDC to induce a nanocavity in PhC and simultaneously couple its exciton emission to the cavity. Figure 4a shows an optical micrograph of a MoTe<sub>2</sub> hybrid nanocavity device. The flake is about 6–8 layers thick based on optical contrast and the PL peak position. The lateral width of the flake along the waveguide is about  $6a$ . Despite not fully covering the PhC along the  $y$ -direction, the transmission spectra taken before and after MoTe<sub>2</sub> flake transfer (Supporting Information Figure S5) indicate that the flake managed to induce the formation of a cavity. Multiple peaks are visible in the transmission spectrum (Figure 4b) with  $Q$  factors of the order of  $10^3$  to  $10^4$ . The lower  $Q$  factors are due to a combination of the larger flake refractive index, the small lateral width, and the absorption by the flake. Modeling a structure with similar properties as the actual device in FDTD and FEM simulations, we confirmed that the formation of the cavity that could support multiple modes is indeed possible (Supporting Information Figure S5). In fact, a local refractive index modulation of a small area adjacent to the waveguide is sufficient to induce strong optical confinement (Supporting Information Figure S6).

A broad background of MoTe<sub>2</sub> exciton emission can be seen in the PL spectrum (Figure 4c). Peaks close to 1200 nm correspond to the Fabry–Perot-like emission arising from the odd guided mode, while the narrow peaks at around 1310 nm correspond to the cavity modes. The bright intensity of these peaks indicates that the MoTe<sub>2</sub> emission is indeed coupled to and enhanced by the cavity. We further performed time-resolved PL measurements. A comparison of the decay curves of the PL from the cavity and bare MoTe<sub>2</sub> (positions 1 and 2, respectively, in Figure 4a) is shown in Figure 4d. From the decay curves, the bare MoTe<sub>2</sub> PL lifetime is extracted to be  $46.1 \pm 0.3$  ps, whereas the cavity emission lifetime is  $3.0 \pm 0.6$  ps. The cavity decay curve is largely similar to that of the instrument response function (IRF), suggesting that the actual lifetime is shorter than the extracted value. Nonetheless, the PL lifetimes indicate an enhancement factor of  $15 \pm 3$ . Our results unambiguously show that the spatial self-alignment of the flake to the nanocavity facilitates light–matter coupling.

## DISCUSSION

We have successfully fabricated hybrid nanocavities using hBN, WSe<sub>2</sub>, and MoTe<sub>2</sub> which exhibit high  $Q$  factor values. A summary of all the fabricated devices is presented in Figure S10 and Supporting Information Table S1. The cavity modes consistently appear at the location of the flakes, indicating that they are not caused by disorder in the PhC waveguide. It is worth reiterating that the extracted  $Q$  factors are  $Q_i$ , which is limited by either  $Q_c$  or  $Q_r$ . The  $Q_i$  is in turn determined only by

the coupling losses to free space and is comprised of the theoretical ( $Q_{th}$ ) and experimental ( $Q_{ex}$ ) losses:  $\frac{1}{Q_i} = \frac{1}{Q_{th}} + \frac{1}{Q_{ex}}$ . The experimental  $Q$  factors of the devices are lower than the theoretical values due to fluctuations in the fabricated structure parameters, for example, nonuniformity of air hole radii and lattice period, leading to scattering losses. The broken vertical symmetry of the device could also contribute to loss via the coupling of transverse electric and transverse magnetic modes.<sup>44,45</sup> The irregular shape of the flake could also lead to losses as more of the flake edges overlap with the air holes.<sup>46</sup> Wrinkles, bubbles, and contaminants could also lead to air gaps between the 2D material flake and the PhC waveguide, affecting cavity  $Q$ . Nonetheless, the surface roughness of the flakes is mostly smooth and the interface between the flake and the PhC substrate is clean, especially for the WSe<sub>2</sub> devices which are fabricated using the anthracene-assisted transfer method.<sup>47</sup> As such, the surface condition of the flake is likely not the main factor that affects the  $Q$  factor. From the scanning electron micrograph of the fabricated PhC waveguide (Supporting Information Figure S7), the PhC air holes show imperfect roundness with slight ellipticity, which we believe to be the main cause that limits the experimental  $Q$  factors.

Despite these issues, high  $Q$  factors have been achieved in our 2D material-induced hybrid PhC nanocavities. The high  $Q/V_{mode}$  of our hybrid nanocavity devices also enabled the observation of nonlinear effects such as the optical bistability at low excitation powers (Supporting Information Note 2 and Figure S8). Recently, there is a study reporting the demonstration of nonlinear frequency conversion using such self-aligned hybrid nanocavities.<sup>48</sup> By comparing the experimentally observed guided mode red shift caused by the 2D materials and the required change in the slab refractive index of the bare PhC waveguide to produce the same red shift in FDTD simulations, it is estimated that a monolayer flake results in 0.1–0.2% change in the local refractive index. The small change in the refractive index facilitates the formation of high  $Q$  cavities, consistent with previous numerical modeling results.<sup>40,49</sup> Simulation results in Figures S2 and S6 also imply that hybrid nanocavities can be formed with only a minimal amount of material while achieving high  $Q$  without requiring stringent fine-alignment. 2D materials, with their ease of heterogeneous integration, are uniquely suitable to achieve such small refractive index modulation to form high  $Q$  cavities. The many degrees of freedom in the 2D material flake and the PhC waveguide enable a broad range of  $Q$  factor tunability to tailor to the needs of the application. Furthermore, the devices are stable, with the cavities showing no significant degradation even after being stored in ambient conditions for a time period of several months (see Supporting Information Figure S9).

## CONCLUSIONS

In conclusion, we have experimentally demonstrated self-aligned hybrid nanocavities by dielectric environment engineering with 2D materials. The cavity can be formed at an arbitrary location along a PhC waveguide by integrating suitably sized 2D materials postfabrication. Since the flake is naturally aligned to the cavity, the flake could readily couple to the cavity for stronger light–matter coupling. Even a monolayer flake can provide sufficient local refractive index modulation to induce the formation of a nanocavity. It is worth emphasizing that 2D materials—with their atomic thicknesses

and ease of heterogeneous integration—are uniquely suitable to achieve the small refractive index modulation necessary to form high  $Q$  cavities. Our versatile approach that utilizes dielectric environment engineering can be extended to encompass a wide variety of 2D materials, with prospects of transforming passive PhC waveguides into cavity-enhanced functional components on hybrid photonic integrated circuits.

## METHODS

**Numerical Simulations.** The photonic band structure is calculated using MIT Photonic Bands (MPB),<sup>50</sup> considering a unit cell of the PhC waveguide with periodic boundary conditions in the  $x$ - and  $y$ -directions. The finite-difference time-domain (FDTD) simulations are performed using the open-source package MEEP<sup>51</sup> on a computing cluster. The grid resolution is usually set to at least  $a/24$  or higher depending on the thickness of the simulated 2D materials. With subpixel averaging, we are able to simulate 2D material of thicknesses down to 5 nm and obtain reliable results. Numerical finite element method (FEM) simulations are carried out with COMSOL to simulate PhC structures with mono- to few-layer thick 2D materials. The simulated PhC waveguide consisting of 48 (14) air holes along the  $\Gamma$ - $K$  ( $\Gamma$ - $M$ ) direction is sufficiently large such that any further increase in the size does not change the  $Q$  factor, i.e., the  $Q$  factor is limited only by out-of-plane losses. The type of simulated 2D materials is controlled by setting the value of the dielectric constant, obtained from Laturia et al.<sup>41</sup> We assume a monolayer effective thickness of 0.7 nm in our simulations. Silicon has minimal absorption at the NIR regime, where that cavity mode is. Aside from  $\text{MoTe}_2$ , hBN and  $\text{WSe}_2$  are not expected to have strong absorption in the NIR and thus we do not include absorption losses in the simulations. We also performed simulations using isotropic or anisotropic dielectric constants and found no significant difference in the results.

**Silicon PhC Waveguide Fabrication.** The PhC waveguides are fabricated on a silicon-on-insulator substrate with a 200 nm-thick top silicon layer and a 1  $\mu\text{m}$ -thick buried oxide layer. The PhC pattern is first defined on a resist mask by electron beam lithography, and then the pattern is transferred onto the substrate via inductively coupled plasma using  $\text{C}_4\text{F}_8$  and  $\text{SF}_6$  gases. Following resist removal, the buried oxide layer is etched away using a solution of 20% hydrofluoric acid to form air-suspended PhC waveguide structures.

**2D Material Dry Transfer.** The hBN flakes (NIMS) are prepared on a polydimethylsiloxane (PDMS) sheet (Gelfilm by Gelpak) by mechanical exfoliation of bulk crystals. Suitable flakes are identified using an optical microscope and then transferred onto the target PhC waveguide using a home-built micromanipulator setup.  $\text{MoTe}_2$  flakes (HQ graphene) are prepared and transferred using the same method.

$\text{WSe}_2$  flakes (HQ graphene) are prepared on commercially available 90 nm-thick  $\text{SiO}_2/\text{Si}$  substrates via mechanical exfoliation to enable the identification of the layer number via optical contrast. The  $\text{WSe}_2$  flakes are then placed on the PhC waveguides using the anthracene-assisted transfer process.<sup>47</sup> To grow the anthracene crystals, anthracene powder is heated to about 80 °C. The sublimated anthracene vapor will then recrystallize on the bottom surface of a glass slide placed at about 1 mm above the anthracene powder. The growth time is typically 10 h. A small PDMS sheet is then placed on a glass slide, followed by an anthracene crystal on the PDMS to form an anthracene/PDMS stamp. Next, this stamp is used to pick

up the  $\text{WSe}_2$  flake. The  $\text{WSe}_2$  flake and anthracene crystal were then transferred together onto the target PhC waveguide. Finally, the anthracene crystal is heated to about 80 °C or left in ambient conditions to sublime, leaving behind clean flakes.

**Optical Spectroscopy.** PL measurements are performed with a home-built confocal microscopy system. A Ti/sapphire laser (Spectra Physics 3900S) is used for excitation, usually at a wavelength of 760–780 nm. The excitation power is controlled using neutral density filters, while the polarization of the laser is adjusted using a half-wave plate to match the polarization of the cavity mode. The laser beam is focused on the samples using an objective lens (Olympus) of 50 $\times$  magnification with a numerical aperture (NA) of 0.65. The emission from the sample is collected with the same objective lens, directed to a spectrometer (Princeton Instruments Acton SP2300), dispersed by a 150 lines/mm grating, and then detected with a liquid nitrogen-cooled InGaAs detector (Princeton Instruments PyLoN IR).

For transmission measurements, a wavelength-tunable continuous-wave laser (Santec TSL-550) is used. A steering mirror and a 4 $f$  system are used to displace the laser excitation spot while keeping the same detection spot. The light scattered from the sample is collected by the objective lens and coupled into an optical fiber to direct the signal to a photoreceiver (New Focus 2011).

For time-resolved measurements, a Ti/sapphire laser (Coherent MIRA) operating in pulsed mode is used for excitation. The excitation wavelength is set to 780 nm. The laser beam is focused on the sample with an objective lens (Olympus) of 100 $\times$  magnification and NA of 0.85. The PL emission is collected by the same objective lens and then filtered spectrally with a long-pass filter to direct light of a specific wavelength range into an optical fiber connected to a superconducting nanowire single-photon detector (Quantum Design Eos). All measurements are carried out at room temperature. The samples are kept in a nitrogen gas environment in order to reduce the oxidation rate of the TMDC flakes.

## ASSOCIATED CONTENT

### Supporting Information

The Supporting Information is available free of charge at <https://pubs.acs.org/doi/10.1021/acsphotonics.3c01927>.

Further simulation results; polarization dependence measurement of the cavity modes; summary of hybrid nanocavity devices; and details of the analysis of the cavity mode intrinsic  $Q$  factor and the optical bistability (PDF)

## AUTHOR INFORMATION

### Corresponding Authors

Chee Fai Fong – Nanoscale Quantum Photonics Laboratory, RIKEN Cluster for Pioneering Research, Saitama 351-0198, Japan; [orcid.org/0000-0003-1676-4665](https://orcid.org/0000-0003-1676-4665); Email: [cheefai.fong@riken.jp](mailto:cheefai.fong@riken.jp)

Yuichiro K. Kato – Nanoscale Quantum Photonics Laboratory, RIKEN Cluster for Pioneering Research, Saitama 351-0198, Japan; Quantum Optoelectronics Research Team, RIKEN Center for Advanced Photonics, Saitama 351-0198, Japan; [orcid.org/0000-0002-9942-1459](https://orcid.org/0000-0002-9942-1459); Email: [yuichiro.kato@riken.jp](mailto:yuichiro.kato@riken.jp)

## Authors

**Daiki Yamashita** – Quantum Optoelectronics Research Team, RIKEN Center for Advanced Photonics, Saitama 351-0198, Japan; Platform Photonics Research Center, National Institute of Advanced Industrial Science and Technology (AIST), Ibaraki 305-8568, Japan; [orcid.org/0000-0002-6970-4677](https://orcid.org/0000-0002-6970-4677)

**Nan Fang** – Nanoscale Quantum Photonics Laboratory, RIKEN Cluster for Pioneering Research, Saitama 351-0198, Japan; [orcid.org/0000-0002-1053-1900](https://orcid.org/0000-0002-1053-1900)

**Shun Fujii** – Quantum Optoelectronics Research Team, RIKEN Center for Advanced Photonics, Saitama 351-0198, Japan; Department of Physics, Faculty of Science and Technology, Keio University, Yokohama 223-8522, Japan; [orcid.org/0000-0002-0998-366X](https://orcid.org/0000-0002-0998-366X)

**Yih-Ren Chang** – Nanoscale Quantum Photonics Laboratory, RIKEN Cluster for Pioneering Research, Saitama 351-0198, Japan

**Takashi Taniguchi** – Research Center for Materials Nanoarchitectonics, National Institute for Materials Science, Tsukuba 305-0044, Japan; [orcid.org/0000-0002-1467-3105](https://orcid.org/0000-0002-1467-3105)

**Kenji Watanabe** – Research Center for Electronic and Optical Materials, National Institute for Materials Science, Tsukuba 305-0044, Japan; [orcid.org/0000-0003-3701-8119](https://orcid.org/0000-0003-3701-8119)

Complete contact information is available at:

<https://pubs.acs.org/10.1021/acsp Photonics.3c01927>

## Author Contributions

C.F.F. conceived the idea and performed the numerical simulations. C.F.F. fabricated the PhC waveguide under the guidance of D.Y. C.F.F. carried out the 2D materials transfer with assistance from N.F. and Y.R.C. C.F.F. performed the optical measurements with some assistance from D.Y. and S.F. K.W. and T.T. provided the bulk hBN crystals. C.F.F. analyzed the data and wrote the manuscript. All authors contributed to the discussion of the results and the manuscript. Y.K.K. supervised the project.

## Notes

The authors declare no competing financial interest.

C.F.F., D.Y., N.F., S.F., Y.-R.C., T.T., K.W., and Y.K.K., Self-Aligned Hybrid Nanocavities Using Atomically Thin Materials. 2023, 2308.10566 arXiv <http://arxiv.org/abs/2308.10566> (accessed May 8, 2024).

## ACKNOWLEDGMENTS

This work was supported in part by JSPS KAKENHI (JP22K14623, JP20H02558, JP20J00817, JP22K14624, JP22K14625, JP22KF0407, JP23H00262, JP24K08296, and JP24K17627) and ARIM of MEXT (JPMXP1222UT1138), as well as the RIKEN Incentive Research Projects. K.W. and T.T. acknowledge support from the JSPS KAKENHI (grant nos. JP21H05233 and JP23H02052) and World Premier International Research Center Initiative (WPI), MEXT, Japan. C.F.F. was supported by the RIKEN SPDR fellowship. Y.-R.C. was supported by the JSPS Postdoctoral Fellowship. We acknowledge support by the RIKEN Information Systems Division for the use of the Supercomputer HOKUSAI BigWaterfall and SailingShip, as well as the use of the COMSOL license.

## REFERENCES

- (1) Xu, X.; Yao, W.; Xiao, D.; Heinz, T. F. Spin and pseudospins in layered transition metal dichalcogenides. *Nat. Phys.* **2014**, *10*, 343–350.
- (2) Krasnok, A.; Lepeshov, S.; Alú, A. Nanophotonics with 2D transition metal dichalcogenides [Invited]. *Opt. Express* **2018**, *26*, 15972.
- (3) Kim, S.; Fröch, J. E.; Christian, J.; Straw, M.; Bishop, J.; Totonjian, D.; Watanabe, K.; Taniguchi, T.; Toth, M.; Aharonovich, I. Photonic crystal cavities from hexagonal boron nitride. *Nat. Commun.* **2018**, *9*, 2623.
- (4) Liu, X.; Hersam, M. C. 2D materials for quantum information science. *Nat. Rev. Mater.* **2019**, *4*, 669–684.
- (5) He, F.; Zhou, Y.; Ye, Z.; Cho, S.-H.; Jeong, J.; Meng, X.; Wang, Y. Moiré Patterns in 2D Materials: A Review. *ACS Nano* **2021**, *15*, 5944–5958.
- (6) Turunen, M.; Brotons-Gisbert, M.; Dai, Y.; Wang, Y.; Scerri, E.; Bonato, C.; Jöns, K. D.; Sun, Z.; Gerardot, B. D. Quantum photonics with layered 2D materials. *Nat. Rev. Phys.* **2022**, *4*, 219–236.
- (7) Montblanch, A. R.-P.; Barbone, M.; Aharonovich, I.; Atatüre, M.; Ferrari, A. C. Layered materials as a platform for quantum technologies. *Nat. Nanotechnol.* **2023**, *18*, 555–571.
- (8) Mak, K. F.; Lee, C.; Hone, J.; Shan, J.; Heinz, T. F. Atomically Thin MoS<sub>2</sub>: A New Direct-Gap Semiconductor. *Phys. Rev. Lett.* **2010**, *105*, 136805.
- (9) Ruppert, C.; Aslan, B.; Heinz, T. F. Optical Properties and Band Gap of Single- and Few-Layer MoTe<sub>2</sub> Crystals. *Nano Lett.* **2014**, *14*, 6231–6236.
- (10) Zhu, B.; Chen, X.; Cui, X. Exciton Binding Energy of Monolayer WS<sub>2</sub>. *Sci. Rep.* **2015**, *5*, 9218.
- (11) Autere, A.; Jussila, H.; Dai, Y.; Wang, Y.; Lipsanen, H.; Sun, Z. Nonlinear Optics with 2D Layered Materials. *Adv. Mater.* **2018**, *30*, 1705963.
- (12) Seyler, K. L.; Schaibley, J. R.; Gong, P.; Rivera, P.; Jones, A. M.; Wu, S.; Yan, J.; Mandrus, D. G.; Yao, W.; Xu, X. Electrical control of second-harmonic generation in a WSe<sub>2</sub> monolayer transistor. *Nat. Nanotechnol.* **2015**, *10*, 407–411.
- (13) Zhang, D.; Zeng, Z.; Tong, Q.; Jiang, Y.; Chen, S.; Zheng, B.; Qu, J.; Li, F.; Zheng, W.; Jiang, F.; Zhao, H.; Huang, L.; Braun, K.; Meixner, A. J.; Wang, X.; Pan, A. Near-Unity Polarization of Valley-Dependent Second-Harmonic Generation in Stacked TMDC Layers and Heterostructures at Room Temperature. *Adv. Mater.* **2020**, *32*, 1908061.
- (14) Hötger, A.; Amit, T.; Klein, J.; Barthelmi, K.; Pelini, T.; Delhomme, A.; Rey, S.; Potemski, M.; Faugeras, C.; Cohen, G.; Hernangómez-Pérez, D.; Taniguchi, T.; Watanabe, K.; Kastl, G.; Finley, J. J.; Refaely-Abramson, S.; Holleitner, A. W.; Stier, A. V. Spin-defect characteristics of single sulfur vacancies in monolayer MoS<sub>2</sub>. *npj 2D Mater. Appl.* **2023**, *7*, 30.
- (15) Gu, T.; Petrone, N.; McMillan, J. F.; van der Zande, A.; Yu, M.; Lo, G. Q.; Kwong, D. L.; Hone, J.; Wong, C. W. Regenerative oscillation and four-wave mixing in graphene optoelectronics. *Nat. Photonics* **2012**, *6*, 554–559.
- (16) Gan, X.; Mak, K. F.; Gao, Y.; You, Y.; Hatami, F.; Hone, J.; Heinz, T. F.; Englund, D. Strong Enhancement of Light–Matter Interaction in Graphene Coupled to a Photonic Crystal Nanocavity. *Nano Lett.* **2012**, *12*, 5626–5631.
- (17) Hammer, S.; Mangold, H. M.; Nguyen, A. E.; Martinez-Ta, D.; Naghibi Alvililar, S.; Bartels, L.; Krenner, H. J. Scalable and Transfer-Free Fabrication of MoS<sub>2</sub>/SiO<sub>2</sub> Hybrid Nanophotonic Cavity Arrays with Quality Factors Exceeding 4000. *Sci. Rep.* **2017**, *7*, 7251.
- (18) Sortino, L.; Zotev, P. G.; Mignuzzi, S.; Cambiasso, J.; Schmidt, D.; Genco, A.; Aßmann, M.; Bayer, M.; Maier, S. A.; Sapienza, R.; Tartakovskii, A. I. Enhanced light-matter interaction in an atomically thin semiconductor coupled with dielectric nano-antennas. *Nat. Commun.* **2019**, *10*, 5119.
- (19) Ge, X.; Minkov, M.; Fan, S.; Li, X.; Zhou, W. Laterally confined photonic crystal surface emitting laser incorporating monolayer tungsten disulfide. *npj 2D Mater. Appl.* **2019**, *3*, 16.

- (20) Fröch, J. E.; Kim, S.; Mendelson, N.; Kianinia, M.; Toth, M.; Aharonovich, I. Coupling Hexagonal Boron Nitride Quantum Emitters to Photonic Crystal Cavities. *ACS Nano* **2020**, *14*, 7085–7091.
- (21) Ono, M.; Hata, M.; Tsunekawa, M.; Nozaki, K.; Sumikura, H.; Chiba, H.; Notomi, M. Ultrafast and energy-efficient all-optical switching with graphene-loaded deep-subwavelength plasmonic waveguides. *Nat. Photonics* **2020**, *14*, 37–43.
- (22) Maiti, R.; Patil, C.; Saadi, M. a. S. R.; Xie, T.; Azadani, J. G.; Uluutku, B.; Amin, R.; Briggs, A. F.; Miscuglio, M.; Van Thourhout, D.; Solares, S. D.; Low, T.; Agarwal, R.; Bank, S. R.; Sorger, V. J. Strain-engineered high-responsivity  $\text{MoTe}_2$  photodetector for silicon photonic integrated circuits. *Nat. Photonics* **2020**, *14*, 578–584.
- (23) Fang, N.; Yamashita, D.; Fujii, S.; Otsuka, K.; Taniguchi, T.; Watanabe, K.; Nagashio, K.; Kato, Y. K. Quantization of Mode Shifts in Nanocavities Integrated with Atomically Thin Sheets. *Adv. Opt. Mater.* **2022**, *10*, 2200538.
- (24) Rosser, D.; Gerace, D.; Chen, Y.; Liu, Y.; Whitehead, J.; Ryou, A.; Andreani, L. C.; Majumdar, A. Dispersive coupling between  $\text{MoSe}_2$  and an integrated zero-dimensional nanocavity. *Opt. Mater. Express* **2022**, *12*, 59.
- (25) Maggiolini, E.; Polimeno, L.; Todisco, F.; Di Renzo, A.; Han, B.; De Giorgi, M.; Ardizzone, V.; Schneider, C.; Mastria, R.; Cannavale, A.; Pugliese, M.; De Marco, L.; Rizzo, A.; Maiorano, V.; Gigli, G.; Gerace, D.; Sanvitto, D.; Ballarini, D. Strongly enhanced light–matter coupling of monolayer  $\text{WS}_2$  from a bound state in the continuum. *Nat. Mater.* **2023**, *22*, 964.
- (26) Gelly, R. J.; White, A. D.; Scuri, G.; Liao, X.; Ahn, G. H.; Deng, B.; Watanabe, K.; Taniguchi, T.; Vučković, J.; Park, H. An Inverse-Designed Nanophotonic Interface for Excitons in Atomically Thin Materials. *Nano Lett.* **2023**, *23*, 8779–8786.
- (27) Azzam, S. I.; Parto, K.; Moody, G. Purcell enhancement and polarization control of single-photon emitters in monolayer  $\text{WSe}_2$  using dielectric nanoantennas. *Nanophotonics* **2023**, *12*, 477–484.
- (28) Wu, S.; Buckley, S.; Schaibley, J. R.; Feng, L.; Yan, J.; Mandrus, D. G.; Hatami, F.; Yao, W.; Vučković, J.; Majumdar, A.; Xu, X. Monolayer semiconductor nanocavity lasers with ultralow thresholds. *Nature* **2015**, *520*, 69–72.
- (29) Li, Y.; Zhang, J.; Huang, D.; Sun, H.; Fan, F.; Feng, J.; Wang, Z.; Ning, C. Z. Room-temperature continuous-wave lasing from monolayer molybdenum ditelluride integrated with a silicon nanobeam cavity. *Nat. Nanotechnol.* **2017**, *12*, 987–992.
- (30) Qian, C.; Troue, M.; Figueiredo, J.; Soubelet, P.; Villafañe, V.; Beierlein, J.; Klemmt, S.; Stier, A. V.; Höfling, S.; Holleitner, A. W.; Finley, J. J. Lasing of moiré trapped  $\text{MoSe}_2/\text{WSe}_2$  interlayer excitons coupled to a nanocavity. *Sci. Adv.* **2024**, *10*, No. eadk6359.
- (31) Peyskens, F.; Chakraborty, C.; Muneeb, M.; Van Thourhout, D.; Englund, D. Integration of single photon emitters in 2D layered materials with a silicon nitride photonic chip. *Nat. Commun.* **2019**, *10*, 4435.
- (32) Kim, S.; Duong, N. M. H.; Nguyen, M.; Lu, T.-J.; Kianinia, M.; Mendelson, N.; Solntsev, A.; Bradac, C.; Englund, D. R.; Aharonovich, I. Integrated on Chip Platform with Quantum Emitters in Layered Materials. *Adv. Opt. Mater.* **2019**, *7*, 1901132.
- (33) Bie, Y.-Q.; Grosso, G.; Heuck, M.; Furchi, M. M.; Cao, Y.; Zheng, J.; Bunandar, D.; Navarro-Moratalla, E.; Zhou, L.; Efetov, D. K.; Taniguchi, T.; Watanabe, K.; Kong, J.; Englund, D.; Jarillo-Herrero, P. A  $\text{MoTe}_2$ -based light-emitting diode and photodetector for silicon photonic integrated circuits. *Nat. Nanotechnol.* **2017**, *12*, 1124–1129.
- (34) Li, C.; Tian, R.; Yi, R.; Hu, S.; Chen, Y.; Yuan, Q.; Zhang, X.; Liu, Y.; Hao, Y.; Gan, X.; Zhao, J.  $\text{MoTe}_2$  PN Homojunction Constructed on a Silicon Photonic Crystal Cavity for High-Performance Photodetector. *ACS Photonics* **2021**, *8*, 2431–2439.
- (35) Song, B.-S.; Noda, S.; Asano, T.; Akahane, Y. Ultra-high-Q photonic double-heterostructure nanocavity. *Nat. Mater.* **2005**, *4*, 207–210.
- (36) Nomura, M.; Kumagai, N.; Iwamoto, S.; Ota, Y.; Arakawa, Y. Laser oscillation in a strongly coupled single-quantum-dot–nanocavity system. *Nat. Phys.* **2010**, *6*, 279–283.
- (37) Kuruma, K.; Ota, Y.; Kakuda, M.; Iwamoto, S.; Arakawa, Y. Time-resolved vacuum Rabi oscillations in a quantum-dot–nanocavity system. *Phys. Rev. B* **2018**, *97*, 235448.
- (38) Wu, S.; Buckley, S.; Jones, A. M.; Ross, J. S.; Ghimire, N. J.; Yan, J.; Mandrus, D. G.; Yao, W.; Hatami, F.; Vučković, J.; Majumdar, A.; Xu, X. Control of two-dimensional excitonic light emission via photonic crystal. *2D Mater.* **2014**, *1*, 011001.
- (39) Ota, Y.; Moriya, R.; Yabuki, N.; Arai, M.; Kakuda, M.; Iwamoto, S.; Machida, T.; Arakawa, Y. Optical coupling between atomically thin black phosphorus and a two dimensional photonic crystal nanocavity. *Appl. Phys. Lett.* **2017**, *110*, 223105.
- (40) Notomi, M.; Taniyama, H. On-demand ultrahigh-Q cavity formation and photon pinning via dynamic waveguide tuning. *Opt. Express* **2008**, *16*, 18657.
- (41) Laturia, A.; Van de Put, M. L.; Vandenberghe, W. G. Dielectric properties of hexagonal boron nitride and transition metal dichalcogenides: From monolayer to bulk. *npj 2D Mater. Appl.* **2018**, *2*, 6.
- (42) Akahane, Y.; Asano, T.; Song, B.-S.; Noda, S. Fine-tuned high-Q photonic-crystal nanocavity. *Opt. Express* **2005**, *13*, 1202.
- (43) Galli, M.; Portalupi, S. L.; Belotti, M.; Andreani, L. C.; O’Faolain, L.; Krauss, T. F. Light scattering and Fano resonances in high-Q photonic crystal nanocavities. *Appl. Phys. Lett.* **2009**, *94*, 071101.
- (44) Kuramochi, E.; Notomi, M.; Hughes, S.; Shinya, A.; Watanabe, T.; Ramunno, L. Disorder-induced scattering loss of line-defect waveguides in photonic crystal slabs. *Phys. Rev. B: Condens. Matter Phys.* **2005**, *72*, 161318.
- (45) Tanaka, Y.; Asano, T.; Hatsuta, R.; Noda, S. Investigation of point-defect cavity formed in two-dimensional photonic crystal slab with one-sided dielectric cladding. *Appl. Phys. Lett.* **2006**, *88*, 011112.
- (46) Tomljenovic-Hanic, S.; de Sterke, C. M.; Steel, M. J.; Eggleton, B. J.; Tanaka, Y.; Noda, S. High-Q cavities in multilayer photonic crystal slabs. *Opt. Express* **2007**, *15*, 17248.
- (47) Otsuka, K.; Fang, N.; Yamashita, D.; Taniguchi, T.; Watanabe, K.; Kato, Y. K. Deterministic transfer of optical-quality carbon nanotubes for atomically defined technology. *Nat. Commun.* **2021**, *12*, 3138.
- (48) Chen, X.; Zhang, Y.; Ji, Y.; Zhang, Y.; Wang, J.; Wu, X.; Zhao, C.; Fang, L.; Jiang, B.; Zhao, J.; Gan, X. Microcavity induced by few-layer GaSe crystal on silicon photonic crystal waveguide for efficient optical frequency conversion. *arXiv* **2024**, arXiv:2403.01434.
- (49) Chiba, H.; Notomi, M. Reconfigurable nanocavity formation in graphene-loaded Si photonic crystal structures. *Opt. Express* **2019**, *27*, 37952.
- (50) Johnson, S. G.; Joannopoulos, J. D. Block-iterative frequency-domain methods for Maxwell’s equations in a planewave basis. *Opt. Express* **2001**, *8*, 173.
- (51) Oskooi, A. F.; Roundy, D.; Ibanescu, M.; Bermel, P.; Joannopoulos, J.; Johnson, S. G. MEEP: A flexible free-software package for electromagnetic simulations by the FDTD method. *Comput. Phys. Commun.* **2010**, *181*, 687–702.